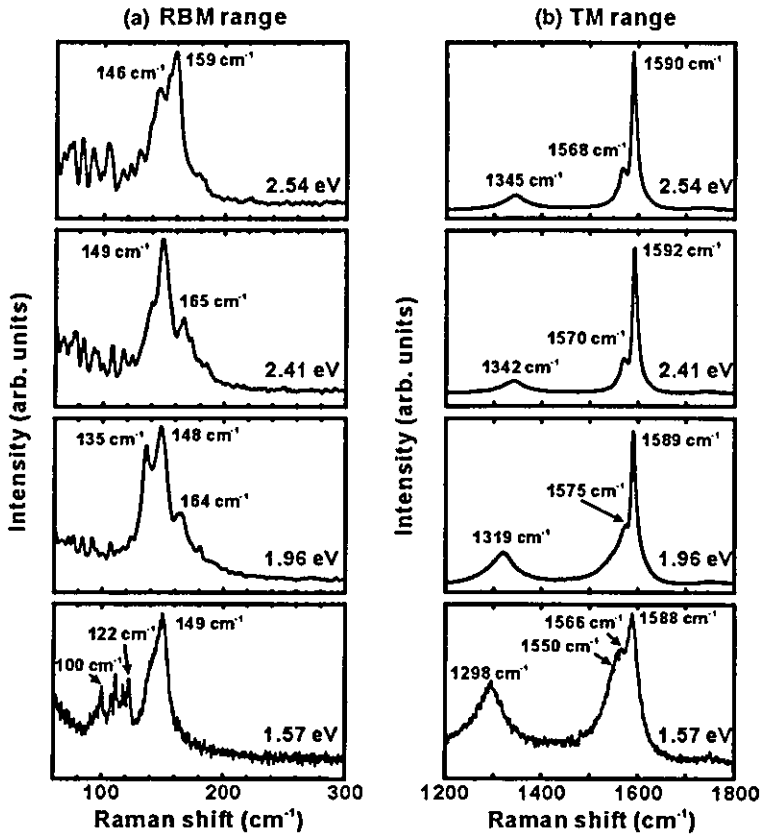

Fig. 3. Raman spectra in (a) RBM and (b) TM ranges using exciting laser with various photon energies for the soot synthesized at Ce concentration of 1.7 at.%, He 500 Torr and arc-discharge current of 70 A and subsequently burned in the air at 533 K for 1 h.

and a shoulder around 1550 cm^{-1} was observed. According to the relationship between diameter and the allowed optical transitions (transfer integral 2.9 eV) derived from band structure calculation based on the tight binding approximation [13,26], a SWCNT with a diameter of 1.5–1.6 nm will be exited by the incident light with energies 1.96, 2.41 and 2.54 eV only when the nanotube is a semiconductor. On the other hand, the metallic nanotube will be exited by an incident light of 1.57 eV. In the TM range, the shape of Raman spectra depends on the laser energy [27–29] and the splitting of the spectra into narrow and symmetric lines is assigned to the resonance from semiconducting SWCNTs, while the broad and asymmetric BFW lineshape type peak [13,30] that centered around 1550 cm^{-1} was assigned to the resonance from the metallic SWCNTs. Therefore, the broad lineshape around 1550 cm^{-1} was due to the presence of metallic SWCNTs.

UV–Vis–NIR spectroscopy is an established technique for characterizing the electronic band structure of SWCNTs [13,14,31–34]. Fig. 4 shows the UV–Vis–NIR spectrum of the soot synthesized at a Ce concentration of 1.7 at.%, He gas pressure of 500 Torr and arc-discharge current of 70 A and subsequently burned in air at 533 K for 1 h. The three peaks at 0.64, 1.14 and 1.60 eV were identified after the strong background due to π electron plasmon of two-dimensional carbon was subtracted from the raw data (inset in Fig. 4). By comparing the peak positions with the values calculated based on the zone folding method [26], these features

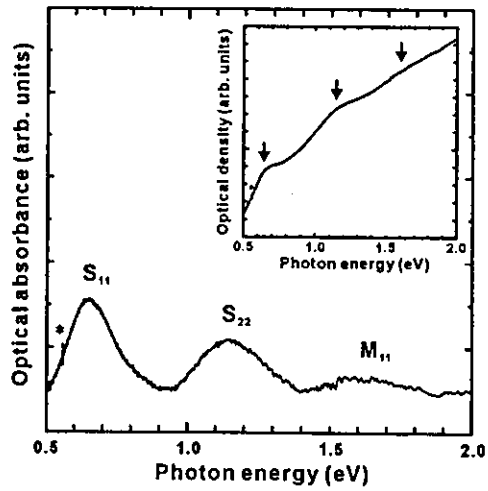

Fig. 4. UV–Vis–NIR spectrum of the soot synthesized at Ce concentration of 1.7 at.%, He 500 Torr and arc-discharge current of 70 A and subsequently burned in the air at 533 K for 1 h. Inset shows the raw UV–Vis–NIR spectrum. Asterisk (*) indicates absorption peak due to the quartz substrate.

were assigned to the allowed optical transitions (transfer integral 2.9 eV) between Van Hove singularities of the density of states in the SWCNT with a diameter of 1.5–1.6 nm. The peaks at 0.64 and 1.14 eV were attributed to the electronic transitions between pairs of singularities in semiconducting SWCNTs ($V_s^1 \rightarrow C_s^1$ and $V_s^2 \rightarrow C_s^2$, respectively), whereas the peak at about 1.60 eV was predominantly from the first pair of singularities ($V_m^1 \rightarrow C_m^1$) in metallic SWCNTs. The appearance of the absorbed energy of the M_{11} band appears at about 1.60 eV confirmed the presence of metallic SWCNTs. This result was in good agreement with the electronic band structure of SWCNTs measured from the Raman scattering spectra. The reason for its appearance at a higher-energy side compared to the calculated S_{11} is due to the Coulomb interaction between SWCNTs [35].

4. Conclusion

We have succeeded in improving the production efficiency of the radial SWCNTs to a value as high as about 20% (by volume from visual inspection of TEM images) using 1.7 at.% of Ce in anode, He gas pressure of 500 Torr and arc-discharge current of 70 A. From the TEM measurement and radial breathing mode of Raman spectra, the average length and diameter of the SWCNTs were determined to be 60 and 1.55 nm, respectively. Also, we have clarified the nature of the electronic structure of the radial SWCNTs. The presence of the metallic and semiconductor type SWCNTs was confirmed from the UV–Vis–NIR spectrum and the tangential mode of Raman spectra. In the carbon materials, conducting amorphous carbon has played an important role on the composites such as the electrode, conducting paints and conducting rubber. The nanotube-filler used in these applications is required to be conducting and easy to disperse in polymer and the nanotubes could be used to form the conducting channel within the polymer. The radial SWCNTs are more easily dispersed in polymer than the semi-finite long SWCNTs. We believe that the radial SWCNTs are applied as the conducting filler.

Acknowledgements

This work was supported by Grant-in-Aid for Basic Research #(S) 14103016 and #(S) 13852016 from the Ministry of Education, Science, Culture and Sport of Japan and #H14-nano-021 from the Ministry of Health, Labor and Welfare. The authors thank Mr. K. Motomiya of Tohoku University, Dr. T. Kamino and Dr. T. Yaguchi of Hitachi Science Systems, Ltd. for their assistance in HRTEM analysis. Y. S. thanks Dr. T. Takenobu of Institute for Materials Research, Tohoku University for useful information and Prof. A. Narayanasamy of University of Madras and Dr. C. N. Chinnasamy of Tohoku University for useful discussion. Also, the authors thank Dr. T. Kochi and Dr. S. Okamoto of HORIBA, Ltd. for the measurement of Raman scattering spectrum and Dr. Yamada of Hitachi Science Systems, Ltd. for the measurement of UV–Vis–NIR spectrum.

References

[1] S. Iijima, T. Ichihashi, Nature 363 (1993) 603.
[2] D.S. Bethune, C.H. Kiang, M.S. de Vries, G. Gorman, R. Savoy, J. Vazquez, R. Beyers, Nature 363 (1993) 605.
[3] A. Thess, R. Lee, P. Nikolaev, H. Dai, P. Petit, J. Robert, C. Xu, Y.H. Lee, S.G. Kim, A.G. Rinzler, D.T. Colbert, G.E. Scuseria, D. Tománek, J.E. Fischer, R.E. Smalley, Science 273 (1996) 483.
[4] K. Tohji, T. Goto, H. Takahashi, Y. Shinoda, N. Shimizu, B. Jeyadevan, I. Matsuoka, Y. Saito, A. Kasuya, T. Ohsuna, K. Hiraga, Y. Nishina, Nature 383 (1996) 679.
[5] J.L. Andrew, G. Rinzler, H. Dai, J.H. Hafner, R.K. Bradley, P.J. Boul, A. Lu, T. Iverson, K. Shelimov, C.B. Huffman, F. Rodriguez-Macias, Y.S. Shon, T.R. Lee, D.T. Colbert, R.E. Smalley, Science 280 (1998) 1253.
[6] R.H. Baughman, A.A. Zakhidov, W.A. de Heer, Science 297 (2002) 787.
[7] S.J. Tans, M.H. Devoret, H. Dai, A. Thess, R.E. Smalley, L.J. Geerligs, C. Dekker, Nature 386 (1997) 474.
[8] H. Dai, Acc. Chem. Res. 35 (2002) 1035.
[9] A. Modi, N. Koratkar, E. Lass, B. Wei, P.M. Ajayan, Nature 424 (2003) 171.
[10] R. Saito, G. Dresselhaus, M.S. Dresselhaus, Physical Properties of Carbon Nanotubes, Imperial College Press, London, 1998.
[11] S. Niyogi, M.A. Hamon, H. Hu, B. Zhao, P. Bhowmik, R. Sen, M.E. Itkis, R.C. Haddon, Acc. Chem. Res. 35 (2002) 1105.
[12] M.F. Yu, B.S. Files, S. Arepalli, R.S. Ruoff, Phys. Rev. Lett. 84 (2000) 5552.
[13] H. Kataura, Y. Kumazawa, Y. Maniwa, I. Umezu, S. Suzuki, Y. Ohtsuka, Y. Achiba, Synth. Met. 103 (1999) 2555.
[14] H. Kuzmany, W. Plank, M. Hulman, C. Kramberger, A. Grüneis, T. Pichler, H. Peterlik, H. Kataura, Y. Achiba, Eur. Phys. J. B 22 (2001) 307.
[15] S. Subramoney, R.S. Ruoff, D.C. Lorents, R. Malhotra, Nature 366 (1993) 637.
[16] D. Zhou, S. Seraphin, S. Wang, Appl. Phys. Lett. 65 (1994) 1593.
[17] Y. Saito, K. Kawabata, M. Okuda, J. Phys. Chem. 99 (1995) 16076.
[18] L. Alvarez, T. Guillard, J.L. Sauvajol, G. Flamant, D. Laplaze, Appl. Phys. A 70 (2000) 169.
[19] A. Kasuya, Y. Sasaki, Y. Saito, K. Tohji, Y. Nishina, Phys. Rev. Lett. 78 (1997) 4434.
[20] L. Alvarez, A. Righi, T. Guillard, S. Rols, E. Anglaret, D. Laplaze, J.L. Sauvajol, Chem. Phys. Lett. 316 (2000) 186.
[21] C.G. Suits, J. Appl. Phys. 10 (1939) 728.
[22] W. Finkelnburg, J. Appl. Phys. 20 (1949) 468.
[23] A.L. Phillips (Ed.), Welding Handbook, sixth ed., American Welding Society, New York, 1968 (Sec.1, Chapter 3).
[24] L. Alvarez, T. Guillard, J.L. Sauvajol, G. Flamant, D. Laplaze, Chem. Phys. Lett. 324 (2001) 7.
[25] S.M. Bachilo, M.S. Strano, C. Kittrell, R.H. Hauge, R.E. Smalley, R.B. Weisman, Science 298 (2002) 2361.
[26] S.D.M. Brown, P. Corio, A. Marucci, M.A. Pimenta, M.S. Dresselhaus, G. Dresselhaus, Phys. Rev. B 61 (2000) 7734.

[27] A. Kasuya, M. Sugano, T. Maeda, Y. Saito, K. Tohji, H. Takahashi, Y. Sasaki, M. Fukushima, Y. Nishina, C. Horie, Phys. Rev. B 57 (1998) 4999.
[28] M. Sugano, A. Kasuya, K. Tohji, Y. Saito, Y. Nishina, Chem. Phys. Lett. 292 (1998) 575.
[29] M.A. Pimenta, A. Marucci, S.A. Empedocles, M.G. Bawendi, E.B. Hanlon, A.M. Rao, P.C. Eklund, R.E. Smalley, G. Dresselhaus, M.S. Dresselhaus, Phys. Rev. B 58 (1998) 16016.
[30] Z. Yu, L. Brus, J. Phys. Chem. B 105 (2001) 1123.
[31] J. Chen, M.A. Hamon, H. Hu, Y. Chen, A.M. Rao, P.C. Eklund, R.C. Haddon, Science 282 (1998) 95.
[32] M.E. Itkis, S. Niyogi, M.E. Meng, M.A. Hamon, H. Hu, R.C. Haddon, Nano Lett. 2 (2002) 155.
[33] P. Petit, C. Mathis, C. Journet, P. Bernier, Chem. Phys. Lett. 305 (1999) 370.
[34] S. Kazaoui, N. Minami, R. Jacquemin, H. Kataura, Y. Achiba, Phys. Rev. B 60 (1999) 13339.
[35] M. Ichida, S. Mizuno, Y. Tani, Y. Saito, A. Nakamura, J. Phys. Soc. Jpn. 68 (1999) 3131.

PROCEEDINGS, 1st International Workshop on WATER DYNAMICS
Tohoku University, Sendai, Japan, 17-19 March, 2004

Synthesis of water-soluble fullerenes and their characterization

Y. AKIMOTO[1], K.SHINODA[1], B. JEYADEVAN[1], K. TOHJI[1], K. KAYA[1], T. MATSUMOTO[2], M. WAELCHLI[3], Y. KURODA[3]

1. Graduate School of Environmental Studies, Tohoku University, Sendai, Japan
2. Institute of Multidisciplinary Research for Advanced Materials, Tohoku University, Sendai, Japan
3. Bruker Biospin CO. LTD., Tsukuba, Japan

We report a new and simple method to synthesize water-soluble fullerenes. Here, the fullerene oxides are simply boiled in alkali aqueous solution to obtain water-soluble species. The mass analysis of water-soluble sample confirms the presence of C_{60} suggesting the dissolution of the same in water. Furthermore, the structure of the water-soluble fullerenes was analyzed in detail by using the Fourier transform infrared, ultraviolet- visible analysis and NMR. We expected to arrive at the structure of the water-soluble fullerenes that has the composition of $C_{60}H_{2n}(OH)_{2n}$ from these analyses.

1. Introduction

Water-soluble fullerene derivatives have a great potential in the field of biological and medical applications. For example, C_{60} derivatives have been applied as anti-HIV and anti-cancer reagents. Chiang et al. and Kitazawa et al. have succeeded in producing water-soluble fullerene, $C_{60}(OH)_n$ using two different methods developed separately. Chiang et al. synthesized the water-soluble fullerene by the hydrolysis of ester moieties of a polyorganocarboxylated fullerene derivative "L.Y.Chiang et al (1992) found". On the other hand, Kitazawa et al. reported a more efficient reaction between C_{60} and NaOH aq, and used tetrabutylammonium hydroxide as phase transfer catalyst "K.Kitazawa et al (1993) found". However, the above methods required numerous steps and several reagents and also had some ions associated in the final products, which hampered their use directly. Therefore, we suggest a simple and efficient method to synthesize water-soluble fullerenes utilizing the fullerene oxides and nucleophilic addition.

2. Experiment

C_{60} was overoxidized by bubbling with ozone gas in C_{60} toluene solution. This treatment was continued until the precipitate was formed (about 20 minutes). Then, the precipitate was filtered and dried. Water-soluble fullerene derivatives were synthesized by boiling the precipitate in NaOH aqueous solution. Then, the suspension was filtered to remove insoluble species. The filtrate was treated with ion-exchange resin to remove sodium ions present in the solution and analyzed by MALDI-TOF-MS (Bruker, Reflex Ⅲ), FT-IR (Thermo Nicolet, AVATAR360), ultraviolet-visible spectrophotometer (HITACHI, U-3300), and ^{13}C-, ^{1}H-NMR (Bruker, Cryoprobe AV500). Then, MM calculation was used to predict the orientation of the functional group of fullerene.

3. Results and Discussion

Figure 1 shows the result of the mass analysis of the synthesized water-soluble fullerene. The matrix used 2.5-dihydroxy benzoic acid. In the mass spectrum, the peak of only C_{60} was observed. Therefore, the determination of the number of functional groups in a fullerene is not possible. However, it is expected that water-soluble fullerene derivative retains fullerene cage.

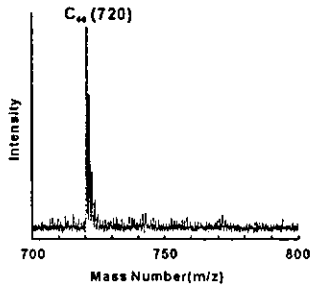

Fig1. Mass spectrum of water-soluble fullerene.

Figure 2 shows the results of IR and UV-vis analysis of water-soluble fullerene. In the IR spectrum, absorption bands corresponding to C-O(1200~1000 cm^{-1}), C-H(about 2900cm^{-1} and 1400cm^{-1}), C=O(about 1700cm^{-1}) and

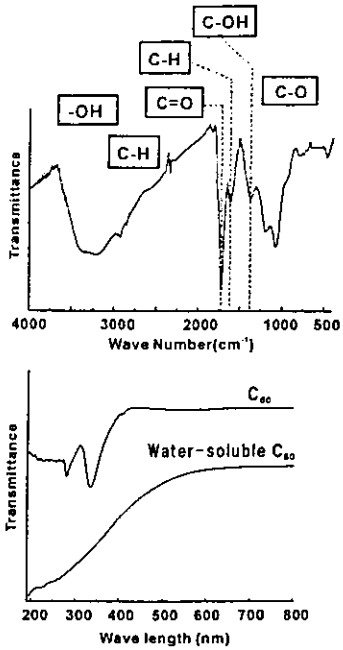

Fig2. IR and UV-vis spectra of water-soluble fullerene

hydroxyl(about 3400cm^{-1} and 1600cm^{-1}) were observed. However, the absorption bands of C_{60} were not observed at all. And also, in the UV-vis spectrum of water-soluble fullerene, the specific absorption band of C_{60} was not observed. The spectrum was broad. It could be expected that this is due to the hydroxyl absorption, which would have drastically changed the natural bonding states of C_{60}.

Figure 3 shows the results of ^{13}C-NMR and ^{1}H-NMR. The ^{13}C-NMR spectrum in D_2O exhibited two signals at about 173, 135 ppm for sp^2 carbons and three signals at about 62, 51 and 33 ppm for sp^3 carbons. The number of peaks in the ^{13}C-NMR spectrum is small. Thus, it is considered that the water-soluble fullerenes have a good structural symmetry. The ^{1}H-NMR spectrum in D_2O exhibited three signals at 4.7, 3.24 and 2.11 ppm. The 4.7 ppm peak is identified with water. The structures expected from the peaks of 2.11 and 3.24 ppm are H-C-C-OH and C-C-(H,OH). The structure of the water-soluble fullerene was considered as follows.

(1) The parts of 6-6 bonds of fullerene are broken.
(2) The functional groups such as proton (-H) and hydroxyl (-OH) ion are attached to the carbon atom in fullerene.
(3) The fullerene derivatives have the composition of $C_{60}H_{2n}(OH)_{2n}$.

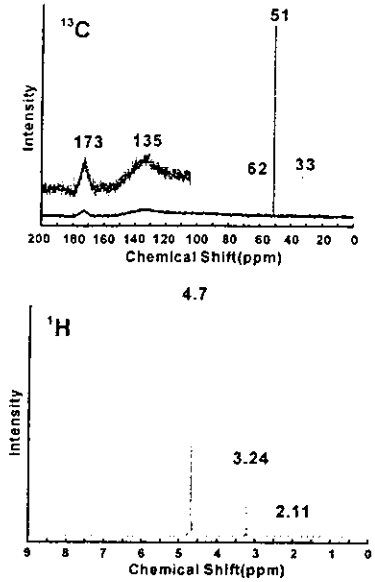

Fig3. ^{13}C- and ^{1}H-NMR spectra of water-soluble fullerene.

Figure 4 shows the optimum model of the water-soluble fullerene, which was calculated by MM. From the results of this calculation, the structure with hydroxyls attached to the symmetrically opposite positions is found to be the stablest.

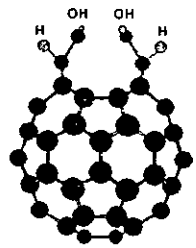

Fig4. The structure expected from MM calculation.

4. Conclusions

The water-soluble fullerene was synthesized by using the fullerene oxides and utilizing the nucleophilic addition reaction. The fullerene derivative with the above unique structure is yet to be reported. Thus we could conclude that we have succeeded in the synthesis of novel fullerene derivative.

References

J.Li, A.Takeuchi, M.Ozawa, X.Li, K.Saigo, K.Kitazawa, *J.Chem.Commun.*, 1993, p.1784

L.Y.Chiang, R.B.Upasani and J.W.Swirczewski, *J. Am.Chem.Soc.*, 1992, 114, 10154

PROCEEDINGS, 1st International Workshop on WATER DYNAMICS
Tohoku University, Sendai, Japan, 17-19 March, 2004

SYNTHESIS OF FERRITE NANOPARTICLES THROUGH AQUEOUS PROCESS FOR BIOMEDICAL APPLICATIONS

R. JUSTIN JOSEYPHUS[1,2], C. N. CHINNASAMY[1], B. JEYADEVAN[1], A. KASUYA[3], K. SHINODA[1], A. NARAYANASAMY[1,2,3], K. TOHJI[1]

[1]Graduate School of Environmental Studies, Tohoku University, Aoba-ku, Sendai 980-8579, Japan
[2]Materials Science Centre, Department of Nuclear Physics, University of Madras, Chennai 600 025, India
[3]Center for Interdisciplinary Research, Tohoku University, Sendai 980-8578, Japan

SUMMARY - The magnetic properties of materials deteriorate when the particle size reaches the superparamagnetic limit and hence it is important to have an appropriate particle size depending on the end use. In this paper we describe the synthesis of manganese zinc ferrite through aqueous process. Oxidation method has been employed through acqueous process to achieve large particles with high magnetization at low temperatures compared to other chemical methods. The synthesis conditions have been optimized to maximize the magnetization by increasing the particle size above the superparamagnetic threshold. The optimum concentration of the oxidant required for ferrite synthesis has been found to be 0.08 M of KNO_3 for 0.5 M NaOH. The results show that the largest particle size that could be achieved using the oxidation method is 80 nm and the magnetization is 49 Am^2/kg.

1. INTRODUCTION

Ferrite nanoparticles find important applications in high frequency devices, information storage, heat transfer devices, drug delivery systems and medical diagnostics. Nanosize particles of ferrites can be prepared by using various synthesis techniques namely ball-milling, citrate precursor method, hydrothermal synthesis, coprecipitation and oxidation methods. Mangenese zinc ferrites are useful for ferrofluid and biomedical applications due to low Curie temperature and high magnetization-temperature gradient. The magnetization value depends on the particle size as smaller particle size leads to superparamagnetism and decreases the magnetization.

In order to increase the magnetization the particle size has to be increased. Synthesis of ferrites through ball milling results in agglomerated particles and other methods like hydrothermal method involve high temperatures. Coprecipitation method results in smaller particle size and hence the magnetization value is low since the particle sizes are of the order of 10-20 nanometer and their magnetic properties are also influenced by parameters like cation distribution "Jeyadevan et al (2000)". Oxidation method can be used to synthesise nanoparticles of bigger sizes compared to the coprecipitation technique. However, the largest particle size obtainable with the oxidation method also varies according to the synthesis conditions used. In this paper we describe the synthesis of Mn-Zn ferrite through oxidation method involving low temperature synthesis in an aqueous medium and its magnetic properties with respect to particle size.

2. MATERIALS AND METHODS

Mn-$ZnFe_2O_4$ was synthesized using analytical grade reagents of $Fe_2SO_4.7H_2O$, $MnCl_2.4H_2O$, $ZnSO_4.H_2O$ and adopting the oxidation method. The ratio of Mn^{2+} to Zn^{2+} ions was fixed as 2 for all the experiments. NaOH was used for precipitation and KNO_3 was used as the oxidant. All the chemicals were of purity greater than 99% (Wako). Oxidation method can be used to synthesize larger particles by oxidising the hydoroxide precipitate with an oxidant to convert the ferrous ions to ferric and form the ferrite phase at lower temperatures. Fe, Mn and Zn salts were dissolved separately in water (0.5 L) and allowed to react with NaOH dissolved in the same amount of water. The resulting precipitate was purged with N_2 before heating to prevent atmospheric oxidation. The metal hydroxide precipitate with a pH between 12-13 was oxidized with various amounts of KNO_3 in a water bath at 90 °C with constant mechanical stirring. The duration of the reaction was 2 h. The phases produced were analyzed using X-ray diffraction (XRD). The average grain size was determined using the Scherrer formula. The morphology of the particles was examined using Scanning Electron Microscopy (SEM). The magnetic properties were measured using a Vibrating Sample Magnetometer (VSM).

The basic reaction mechanism of ferrite formation in the simple case of $FeO.Fe_2O_3$ (magnetite) is as follows:

(a) Fe(II) hydrolysis:

$Fe^{2+} + H_2O \rightarrow FeOH^+ + H^+$

(b) Fe(II) oxidation:

$2FeOH^{+} + 1/2\ O_2 + H_2O \rightarrow 2\ Fe(OH)_2^{+}$

(c) Precipitaion of partially oxidized intermediate:

$(2\text{-}x)Fe(OH)_2^{+} + (1+x)Fe(OH)^{+} + xSO_4^{2-} + (3\text{-}2x)OH^{-} \rightarrow (Fe^{3+})_{2-x}(Fe^{2+})_{1+x}(SO_4^{2-})_x(OH^{-})_{8-3x}$

(d) Additional Fe(II) oxidation at constant pH:

$2[(Fe^{3+})_{2-x}(Fe^{2+})_{1+x}(SO_4^{2-})_x(OH^{-})_{8-3x}] + x/2\ O_2 + 5xH_2O \rightarrow 2\ [(Fe^{3+})_{2-x}(Fe^{2+})(OH^{-})_8] + 2xH_2SO_4$

(e) De-hydration and magnetite formation:

$[(Fe^{3+})_{2-x}(Fe^{2+})(OH^{-})_8] \rightarrow FeO.Fe_2O_3 + 4H_2O$

From these reactions, it is seen that the ferrite phase formation occurs by hydrolysis and subsequent dehydration. A similar reaction mechanism takes place in the synthesis of Mn-Zn ferrite also. The ferrite phase formation also depends on the temperature and duration of the reaction. In the case of Mn-Zn ferrites, the temperature of 90 °C and the duration of 2 h were sufficient for the reaction to complete.

Metal salts of 0.17 M are allowed to react with 0.5 M of NaOH. The resulting metal hydroxide precipitate was heated with various moles of KNO_3. The KNO_3 mole values used were 0.05 M, 0.07 M, 0.08 M, 0.09 M, 0.15 M and 0.20 M.

3. RESULTS AND DISCUSSION

Fig.1 shows the XRD of the Mn-$ZnFe_2O_4$ sample with (a) 0.08 M (b) 0.09 M and (c) 0.20 M. The XRD showed the formation of pure spinel phase with increasing moles of KNO_3. The average grain size was found to be in the range of 23-27 nm upto 0.09 M KNO_3 and thereafter decreased to

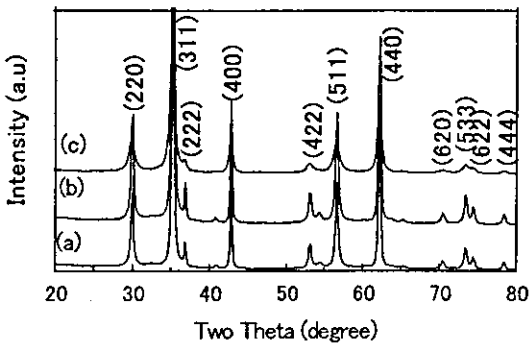

Fig.1. The XRD of the Mn-$ZnFe_2O_4$ sample with KNO_3 of (a) 0.08 M, (b) 0.09 M and (c) 0.20 M.

12 nm for the 0.20 M KNO_3 sample. For the lowest concentration of KNO_3 a small amount of hydroxide impurity peak is observed. Fig.2 shows the SEM photographs of the 0.09 M KNO_3 added sample. It is seen from the SEM results that the average particle size is 80 nm for the samples synthesized with less than 0.09 M of KNO_3 and

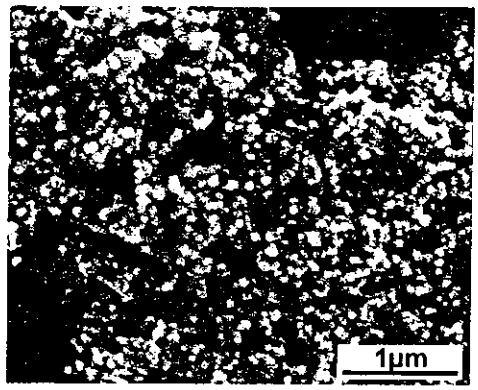

Fig.2. The SEM photograph of the Mn-$ZnFe_2O_4$ synthesized with 0.09 M KNO_3.

the average particle size decreased to less than 20 nm when the KNO_3 was 0.20 M. Fig.3 shows the saturation magnetization as a function of KNO_3 concentration. It is seen that the saturation magnetization is maximum with 49 Am^2/kg for the 0.08 M sample whereas it decreases to 39 Am^2/kg for the 0.20 M of KNO_3 due to reduction of particle size. The Mn-Zn ferrite particles synthesized using coprecipitation method have

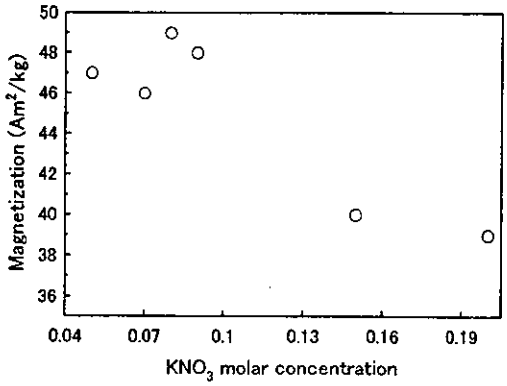

Fig.3. The saturation magnetization of the Mn-$ZnFe_2O_4$ as a function of KNO_3 concentration.

given a magnetization value of 37 Am^2/kg for 9 nm particles as reported by "Jeyadevan *et al* (2003)" whereas with the oxidation method we are able to synthesise 80 nm nanoparticles with a magnetization of 49 Am^2/kg.

4. CONCLUSIONS

Mn-Zn ferrite has been prepared by the oxidation method. The spinel phase formation depends upon the concentration of the oxidant used and the optimum amount of KNO_3 required for the maximum particle size is found to be 0.08 M for a fixed molar concentration of metal salts. The largest magnetization obtained is 49 Am^2/kg for a particle size of 80 nm.

5. ACKNOWLEDGEMENTS

This study was supported by grant-in-aid for basic research B#15360003 from the Ministry of Education, Science, Culture and Sport of Japan.

6. REFERENCES

Jeyadevan, B., Tohji, K., Nakatsuka, K., and Narayanasamy, A. (2000). Irregular distribution of metal ions in ferrites prepared by co-precipitation technique structure analysis of Mn–Zn ferrite using extended X-ray absorption fine structure. *J. Magn. Magn. Mater.*, Vol.217, 99-105.

Jeyadevan, B., Chinnasamy, C. N., Shinoda, K., Tohji, K., and Oka, H. (2003). Mn-Zn ferrite with higher magnetization for temperature sensitive magnetic fluid. *J. Appl. Phys.*, Vol.93, 8450-8452.

カーボンナノチューブの固化とハイドロキシアパタイト被覆

大森守[1)]，大久保昭[1)]，大坪誠[2)]，田路和幸[2)]，橋田俊之[2)]

1）東北大・金研，2）東北大院・工

Consolidation of Multi-Walled Carbon Nanotube and Hydroxyapatite Coating

Mamoru OMORI[1)], Akira OKUBO[1)], Makoto OTUBO[2)], Kazuyuki TOHJI[2)], Toshiyuki HASHIDA[2)]

1) Tohoku University, Institute for Materials Research, Sendai, Japan

2) Tohoku University, Graduate School of Engineering, Sendai, Japan

Abstract

The malti-walled carbon nanotube (MWNT) was coated with phenol resin and consolidated at 1000–1600°C at 120 MPa in a vacuum by the spark plasma system (SPS). The bulk density was between 1.67 g/cm^3 and 1.74 g/cm^3 for the MWNTs consolidated at 1000–1400°C. Young's modulus was 11.1 GPa for the MWNT consolidated at 1200°C and 3.05 GPa for the MWNT consolidated at 1000°C. The consolidated MWNT was put in the suspension made of $6CaHPO_4{\cdot}2H_2O$ and $4Ca(0H)_2$. The coated compounds were heated at 1000°C at 120 MPa in a vacuum by SPS and resulted in the hydroxyapatite film on the consolidated MWNT.

1 はじめに

カーボンナノチューブ(CNT)を固化して材料として使う研究はまだ行われていない。カーボンナノチューブの機械的性質の特徴は軽いことと強度の大きいことである。現時点ではカーボンナノチューブの価格が高いため、それを固化して実際の材料に使うことはできないが、今後の技術開発により価格は急速に低下すると予想される。そうなれば固化したカーボンナノチューブは多くの分野で使われるようになるのは確実である。

固化カーボンナノチューブの軽量性と、黒鉛が生体材料として使われていることに焦点を合わせると、人工骨への応用は注目される課題である。チューブ構造のために、正確なカーボンナノチューブの嵩密度は分からないが 2g/cm^3 以下と考えられる。カーボンナノチューブの引っ張り強度は数十 GPa とも言われて非常に大きいと考えられており、この特徴を引き出して強い材料にするための固化の方法を見つけることが重要な課題である。本研究では放電プラズマ焼結法(SPS)に注目し、この装置の持つ効果を利用してカーボンナノチューブを固化することを試みている。カーボンナノチューブは基本的には黒鉛であり、その焼結性は黒鉛と類似して良くないと考えられる。またカーボンナノチューブは黒鉛とは異なる構造で黒鉛ほどに耐熱性は良くないと考えられる。特に単層カーボンナノチューブ(SWNT)の耐熱性は多層カーボンナノチューブ(MWNT)に比べて劣り、2400°C までには多層カーボンナノチューブに転移すると報告されている[1]。黒鉛の焼結には、2500°C 以上の高い温度が必要であり[2]、この温度では多層カーボンナノチューブも破壊されると考えられる。SPS 法では電場や放電プラズマの効果があり難焼結性の粉体でも焼結できる例が報告されている[3]。この方法を利用してカーボンナノチューブを固化する試みを行った。購

入した多層カーボンナノチューブには約２０％の非晶質炭素が混入している。多層カーボンナノチューブの固化促進のためにフェノール樹脂を添加し固化できたので、その結晶構造を X 線回折法で調べ、機械的性質を測定した。

固化カーボンナノチューブの生体活性は良くないので、これを改善するためにハイドロキシアパタイトの被覆を試みた。ハイドロキシアパタイトは真空中では 1000°C 以上で、大気圧中では 1200°C 近傍から分解が始まる[4]。ハイドロキシアパタイトの被覆を商業的に行うためにプラズマ溶射法が採用されているが、得られた膜は分解生成物となる[5]。また実験的に行われているイオンビームスパッタ法では非晶質の膜となり、それを結晶化するための加熱によって基盤との熱膨張の差によりクラックが発生する[6]。このようにハイドロキシアパタイトの被覆にはまだ成功していない。本研究では、水熱合成法で使われている 6 モルの $CaHPO_4 \cdot 2H_2O$ と 4 モルの $Ca(OH)_2$ との混合原料を使い[7]、その懸濁液を固化カーボンナノチューブに塗布し、SPS によって反応しハイドロキシアパタイト膜とすることを試みた。

2 実験方法

2.1 多層カーボンナノチューブの固化

多層カーボンナノチューブの原料はアメリカのナノラボ社で作られた。この多層カーボンナノチューブの純度は約 80%であり、残りは非晶質炭素である。この原料の固化には住友石炭鉱業製の放電プラズマシステム（SPS1050）を用いた。多層カーボンナノチューブのみを SPS を用いて固化した。さらに、フェノール樹脂をアルコールに溶解し、そこへ多層カーボンナノチューブを加えた。これをよく攪拌し混合してから、アルコールを蒸発させた後 200～300°C の温度でフェノール樹脂を分解して粉末とし、これを 120MPa の加圧のもとで、1000°C から 1600°C の温度範囲で固化した。固化の雰囲気はすべて真空である。

固化カーボンナノチューブの構造を解析するためにX線回折（理学電機、RU-200B）、透過電子顕微鏡（日本電子、JT-007）、光学顕微鏡（ニコン、N-01）および走査型電子顕微鏡（日立、S-800）での測定と観察とを行った。密度はアルキメデス法で調べた。弾性定数は、20mmφで厚さ 3mm の試料を使い、超音波伝搬の時間の測定によって求めた。

2.2 カーボンナノチューブ固化体へハイドロキシアパタイトの被覆

6 モルの $CaHPO_4 \cdot 2H_2O$ と 4 モルの $Ca(OH)_2$ とを混合した原料を、グリコール酸と一緒に水に入れて懸濁液を作った。この懸濁液に固化カーボンナノチューブを漬け表面に膜を作り、これを黒鉛性の型に炭素粉と一緒に入れ、雰囲気を真空にして 120MPa の加圧下で、1000°C まで温度を上げ、その温度に 5 分間保持して被覆を完了した。

3 結果および考察

3.1 多層カーボンナノチューブの固化

原料の多層カーボンナノチューブは、図 1 に示されるようにその直径が 20mμ～40mμが大部分

であるが、直径 200nm の太いチューブも観察される。この多層カーボンナノチューブを SPS 用いて 120MPa の圧力を加え、1000°C の温度にしても固化できなかった。約 20%含まれている非晶質炭素の存在は固化促進には効果がなかった。固化を促進する目的でフェノール樹脂を添加した。このフェノール樹脂を加熱したときの炭素残留量は約 20%である。30%のフェノール樹脂を添加して得られた固化体には大きなポアが存在し、十分に緻密化が進行していないことが分かった。50%添加の固化体の光学顕微鏡写真を図２に示す。この図から分かるように、ポアは無くなりフェノール樹脂の添加量として 50%が適切である。この光学顕微鏡写真は偏向フィルターを使用して撮影されており、ここで観察される組織的不均一性は結晶の配向性の違いによるものである。フェノール樹脂と多層カーボンナノチューブとを混合してから微細に粉砕しており、この写真にあるように固まりで一定の配向を示すように整列するのは固化中においてであり、微細な多層カーボンナノチューブが安定化するために配列してある大きさの固まりになっているとしか考えられない。

図１多層カーボンナノチューブの透過電子顕微鏡写真

構造を調べるために X 線回折を測定し、それを図３に示した。この図に黒鉛の回折ピーク位置を角印で示した。原料の多層カーボンナノチューブの回折図は黒鉛のそれとほとんど同じである。1000°C での固化体の回折図はまだ原料と同じであるが、1200°C と温度を高くすると黒鉛の(101)ピークが他に比べて大きくなり、1400°C ではさらにそれが著しくなっている。この 1400°C で得られた固化体には黒鉛にはない回折ピークが現れ、1600°C での固化でそれがさらに明瞭になっている。新しいピークはこれまでに報告されている黒鉛の結晶のそれと一致せず、新しい炭素の結晶ができている可能性がある。

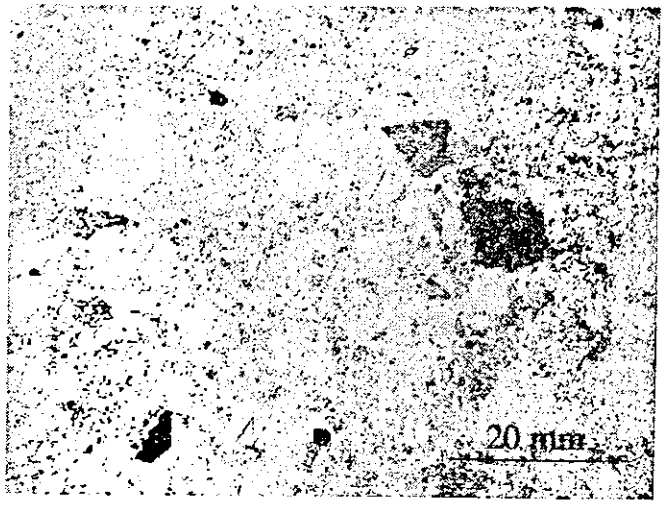

図２フェノール樹脂50%を添加して固化したカーボンナノチューブ

表１には 1000°C、1200°C、1400°C の各温度で得られた固化体の嵩密度、弾性定数、開孔率を示す。嵩密度は 1000°C の固化ではその他のものより低く固化が十分に行われていないと思われる。1200°C での固化では嵩密度

1.74g/cm^3 と一番大きくなっている。人工骨の嵩密度は 1.6～2.1g/cm^3 であり[8]、固化体の嵩密度は人工骨とほぼ同じである。多層カーボンナノチューブはチューブ構造のために黒鉛の理論密度 2.266g/cm^3 より小さいはずであり、正確な値に関する報告はないので相対密度を計算できないが、光学顕微鏡の写真から推定すると90%以上の緻密体になっていると思われる。開孔率はどの固化体でも16%でほぼ同じであり、これはチューブ構造によると考えられる。閉じた孔の割合は黒鉛の論密度から計算しており、多層カーボンナノチューブの理論密度が小さいと考えられるので、これらの値も小さくなるはずである。ヤング率は 1200°C の固化体で 11.1GPa となっている。嵩密度が 2.0g/cm^3 と大きい炭素製品のヤング率が 16GPa であることを考えると、先の固化体のヤング率は小さくはない。人工骨のヤング率が 7～30GPa であり[8]、固化体のヤング率は同じ大きさとなっている。1000°C 固化体のポアソン比が負になっているが、これはこの温度で緻密化が十分に進行していないためである。その他の固化体のポアソン比は小さく、歪みがチューブ構造で吸収されていることが考えられる。曲げ試験を行ったが塑性変形に類似する変形のために測定できなかった。

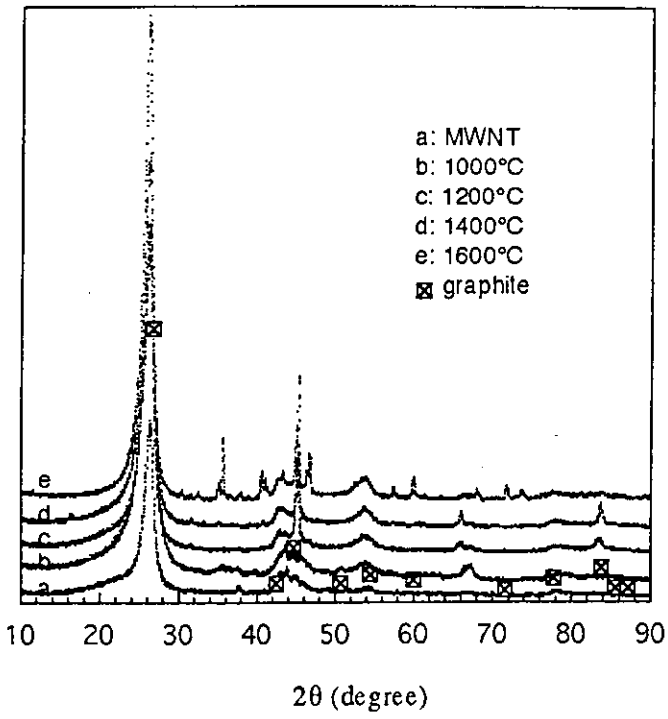

図３多層カーボンナノチューブ(MWNT)と固化体のX線回折図

表１固化したカーボンナノチューブのかさ密度と弾性定数

Consolidation temperature (°C)	Density (g/cm^3)	Apparent porosity (%)	Closed porosiry (%)	Young's modulus (GPa)	Poisson's ratio
1000	1.67	16.7	9.6	3.05	- 0.62
1200	1.74	16.8	6.4	11.1	0.074
1400	1.73	15.6	8.1	10.1	0.034

3.2 ハイドロキシアパタイトの被覆

従来から行われているハイドロキシアパタイトの合成には、原料を酸で溶解し、PH を調整して沈殿を作り、800°C での焼成で結晶を大きくする方法、水蒸気雰囲気で 1200°C で反応させる方法、水熱法で 200°C で析出させる方法の３種類がある[9]。

本研究においては水熱合成で使われる 6 モルの $CaHPO_4 \cdot 2H_2O$ と 4 モルの $Ca(OH)_2$ とを原料にして、これから懸濁液を作りその中に基盤を浸して膜を作り、それを SPS にて反応させてハイドロキシアパタイトを生成させ、同時に基盤と密着させる方法を開発した。6 モルの $CaHPO_4 \cdot 2H_2O$ と 4 モルの $Ca(OH)_2$ との混合原料を、単に 100°C 以上に加熱してもハイドロキシアパタイトは生成しない。SPS 法により 120MPa で 1000°C に加熱することでハイドロキシアパタイトが生成することを見つけた。

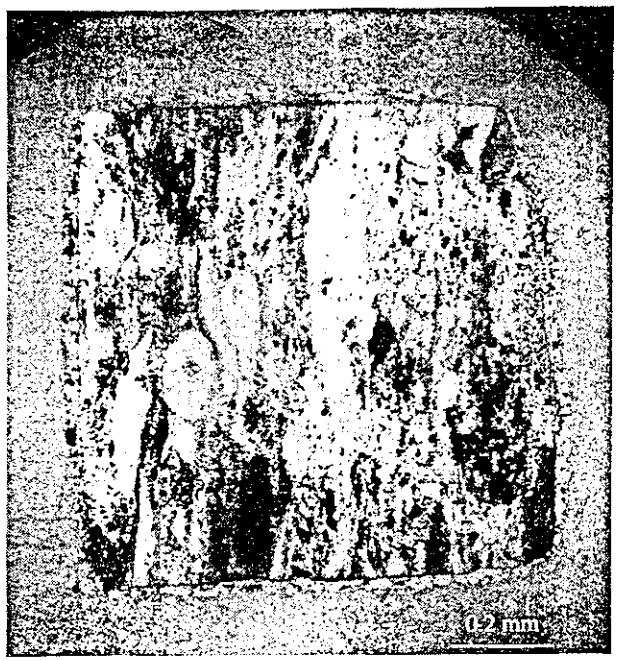

図４ハイドロキシアパタイトを被覆した固化カーボンナノチューブ

多層カーボンナノチューブの固化体上にハイドロキシアパタイトの被覆を 1000°C で試み、加圧力を 120MPa とすると得られたハイドロキシアパタイト膜は密着性がよく剥げ落ちることはなかった。この被覆膜の光学顕微鏡写真を図４に示す。膜にはクラックがなく密着性もよいように見える。切断などの加工を施しても剥げ落ちないことから、かなり密着性のある膜ではないかと推定される。

4 結論

多層カーボンナノチューブの固化を放電プラズマシステム(SPS)によって行った。原料の多層カーボンナノチューブには約 20%の非晶質炭素が含まれているがそのままでは固化されず、フェノール樹脂の添加によって生成する非晶質炭素によって固化できることが分かった。50%の添加で孔のない固化体の作ることができた。固化温度が 1200°C から 1400°C の間で、かさ密度とヤング率が大きくなり、それぞれの値は骨のそれに類似している。この固化カーボンナノチューブの表面を生体活性にするために、6 mol の $CaHPO_4 \cdot 2H_2O$ と 4 mol の $Ca(OH)_2$ との混合原料を使い、その懸濁液を塗布してハイドロキシアパタイト膜生成を SPS で行った。1000°C で 120MPa の条件で密着性がよく割れのない膜を生成するこができた。

謝辞

本研究は、厚生労働科学研究費補助金の萌芽的先端医療技術推進研究事業「ナノチューブ、ナノ微粒子、マイクロ微粒子の組織反応性とバイオ応用」（課題番号 H14-ナノ-021）の助成を受けて行われたもので、ここに感謝の意を表します。また本研究を遂行するに当たり、透過電子顕微鏡観察で協力頂いた伊藤俊氏と、走査型電子顕微鏡観察で協力頂いた村上義弘氏に深謝申し上げます。

参考文献

1) A. Bougrine, N. Dupont-Pavlovsky, A Naji, J. Ghanbaja, J. F. Mareche and D. Billaud: Carbon, 39 (2001), 685.

2) H. Boeder and E. Fitzer: Carbon, 8 (1970), 453.

3) M. Omori: Mater. Sci. Eng., A287 (2000), 183.

4) P. E. Wang and T. K. Chaki: J. Mater. Sci. Mater. Med., 4 (1993) 150.

5) B. KochJ. G. C. Wolke and K. de Groot: J. Biomed. Mater. Res., 24 (1990) 655.

6) J. L. Ong, L. C. Lucas, W. R. Lacefield and E. D. Rigney: Biomater., 13 (1992) 249.

7) K. Hosoi, T. Hashida, H. Takahashi, N. Yamazaki and T. Korenaga: J. Am. Ceram. Soc., 79 (1996), 2771

8) L. H. Hench: J. Am. Ceram. Soc., 81 (1998), 1705.

9) R. Z. LeGeros and J. P. LeGeros: pp. 139-180 in "An Introduction to Bioceramics", World Scientific, London (1993).

カーボンナノチューブ、ナノ・マイクロ微粒子に対する生体反応

○田村一央[1)]，高師則行[1)]，赤坂司[1)]，ロスカ・イオシフ[1)]，
宇尾基弘[1)]，戸塚靖則[1)]，田路和幸[2)]，亘理文夫[1)]
1) 北大院・歯　2)東北大院・工

Pathobiological Response of Carbon nano-tubes and Micro/nano particles

○ Kazuchika TAMURA[1)], Noriyuki TAKASHI[1)], Tukasa AKASAKA[1)], Rosca IOSIF[1)],
Motohiro UO[1)] Yasunori TOTSUKA[1)], Kazuyuki Tohji[2)], Fumio WATARI[1)]
1) Hokkaido University, Graduate School of Dental Medicine, Sapporo, Hokkaido, Japan
2) Tohoku University, Industrial Research Institute, Sendai, Miyagi, Japan

Abstract. The cytotoxicity of micro/nano particles in Ti, TiO_2 and carbon nanotube was investigated by *in vitro* biochemical analyses using human neutrophils. The particles smaller and larger than the neutrophils were used to determine the relationship between cell and particle size with respect to cytotoxicity. As the particle size decreased, the cell survival rate decreased and, with the good corresponding relation to this, the value of lactate dehydrogenase (LDH), which is the indication of cell disruption, was increased. The release of superoxide anion showed the increasing tendency. Proinflammatory cytokines were detected distinctly for 3μm or smaller particles and very little in more than 10μm, which is closely related to the phagocytosis by neutrophils. ICP elemental analysis showed that the dissolution from Ti particles was below detection limit. Micro and nano particles stimulated the cell reactions according to the results of the human neutrophil functional tests. As the particle size was smaller, the inflammation was pronounced. The fine particles less than 3μm caused distinctly the inflammation in the surrounding tissue. All these results indicated that the cytotoxicity was induced due to the physical size effect of particles, which is different from the ionic dissolution effect. The clinical phenomenon confirmed the result obtained *in vitro* cell tests. The neutrophils stimulated by fine particles may cause the inflammatory cascade and harm the surrounding tissue.

Introduction

Titanium (Ti) and its alloys are the commonly used material in plastic surgery because it is one of the most biocompatible metals [1,2]. Ti is highly corrosion-resistant at ambient temperature due to its thin and stable protective oxide layer formed on its surface. In this sense Ti is the ideal metallic material for implant [3,4]. However, it is clinically reported that the abraded fine titanium

particles produced in sliding parts of artificial joints often caused inflammation in the surrounding tissue [1,2]. However, little is known about the effect of micro/nanoparticles on cellular function and the relevance between *in vivo* and *in vitro* findings. The purpose of this study is to analyze the vital reactions of human neutrophils to the Ti, TiO_2 particles and carbon nanotubes and their size effect.

Materials and probe cells

The dependence of cytotoxicity on particles size in Ti, TiO_2 and carbon nanotubes (CNTs) was investigated by biochemical functional analysis and by microscopic observation of cellular morphology.

Particles. The Ti, TiO_2 and CNTs colloid solutions were prepared. ICP elemental analysis showed that the dissolution from Ti particles were below detection limit. The CNTs is 99% purity. The solubilization distributed processing was carried. The average diameter and size distribution of the TiO_2 particles and CNTs were determined by electron microscopy (SEM) and by laser scattering particle distribution analyzer (SALD-7000, Shimadzu). The various sizes of Ti, TiO_2 and CNTs particles were mixed with HBSS (Hanks' balanced salt solution). The colloid solutions were adjusted to pH 6.8 by 1N NaOH solution, sterilized by autoclave and dispersed by sonicator [5,7].

Cells. Human peripheral blood was obtained from healthy volunteers in our group. Neutrophils were separated from the blood using the 6% isotonic sodium chloride containing the hydroxyethyl starch and lymphocyte isolation solution (Ficoll-Hypaque)[6,7]. The cells were maintained in HBSS. After particles were kept dispersed, neutrophils were added, and incubated in a humidified atmosphere of 5% carbon dioxide at 37 °C for 60 minutes. The experiments were performed using cells within 3 hours after collection of blood and the cell density was adjusted to 10^6 cells / ml [7].

Methods

Cell survival rate, leakage of lactate dehydrogenase (LDH), product of superoxide anion, and release of cytokines of tumor necrosis factor-alpha (TNF-alpha), interleukine-1 beta (IL-1beta)) were measured to analyze biochemical reaction.

(1) Cell survival rate: The cell stained with trypan blue population was counted under an optical microscope using Thomas' hemacytometer. The number of vital cell in the control specimen was considered as 100%.

(2) LDH activity: The LDH values of samples were measured using the lactate dehydrogenase C test kit (Wako Pure Chemical Industries) and by spectrophotometry.

(3) Superoxide anion production: Superoxide anion (O_2^-) was assayed by measuring the superoxide dismutase-inhibiting reduction of equine ferricytochrome C (550 nm). The reaction was promoted by adding 1.39mM PMA (phorbol 12-myristate 13-acetate) [7].

(4) Cytokine release: TNF-alpha and IL-1 beta in the supernatant were measured using ELISA kits (Endogen) [7].

The values are expressed as means +/- standard deviation (n=9). Data were analyzed by Student's-t test with the level of significance set at 5%.

The pathological and morphological changes were observed by optical microscopy and SEM.

Results

Ti particles diameter were 3, 10, 50, and 150 μm and TiO_2 particles were 0.05, 0.5, and 3 μm in average size, as confirmed by SEM and the particle distribution analyzer. The SEM image shows CNTs with diameter of 20 nm and length of 100 nm.

Fig.1 shows hypodermal tissue after 5 days with10μm titanium particles, and 3μm particles. Acute inflammation diseases are observed in the both organizations. The strong inflammatory cells infiltrate in the circumference of the particles is recognized in the edema tissue. The left photograph show the titanium particle is scattered in the organization and the inflammatory cells phagocytize them. The size of cells is 10 μ m, the same of titanium particle. Fig.2 shows hypodermal tissue after 2 days with CNTs. The phagocytosis image is not observed. It was not possible to observe the 50nm CNTs in the optical microscope, but it was possible to observe the organization reaction clearly. The peripheral capillaries were congested. Large number of cells permeated in edematous tissue. The significant difference of the survival rate from control was showed in all nanoparticles (Fig.3). The Ti micro particles showed clearly the size dependency. The cell survival rate decreased, when the particle size became smaller. The nanoparticle of TiO_2 also showed the similar tendency. The lowest mean value of the survival rate was 84.6% in the size 50 nm for TiO_2 particles, which were the smallest particles in this study.

LDH showed the tendency to increase as the particle size became smaller (Fig.4). The LDH level of 147.2 Wroblewski unit was significantly higher in the 50 nm than the other larger sizes.

The neutrophils stimulated by the 3 μm or less particles showed the large productions of superoxide anion. The other larger size particles were slightly higher than control solutions (Fig.5).

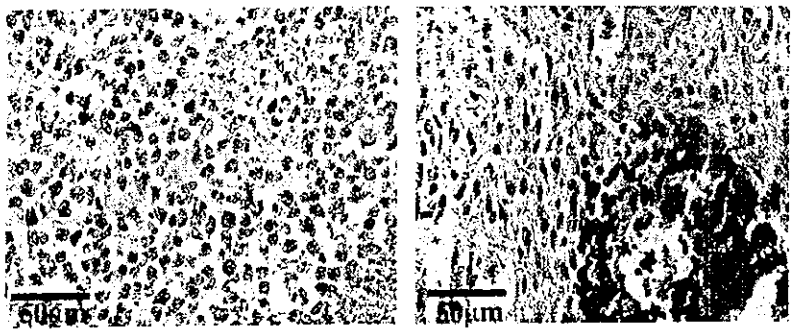

Fig1. Ti particles after 5 days

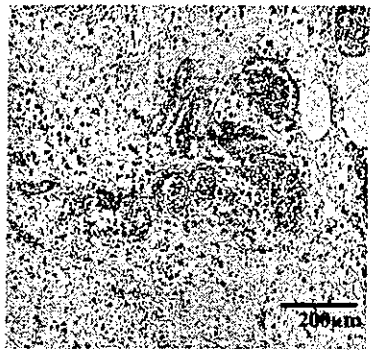

Fig.2 50nm CNT after 2days

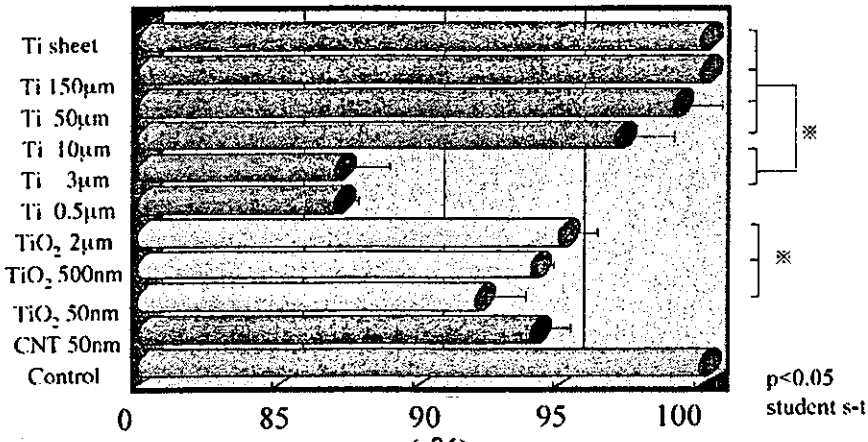

Fig.3 Survival rate

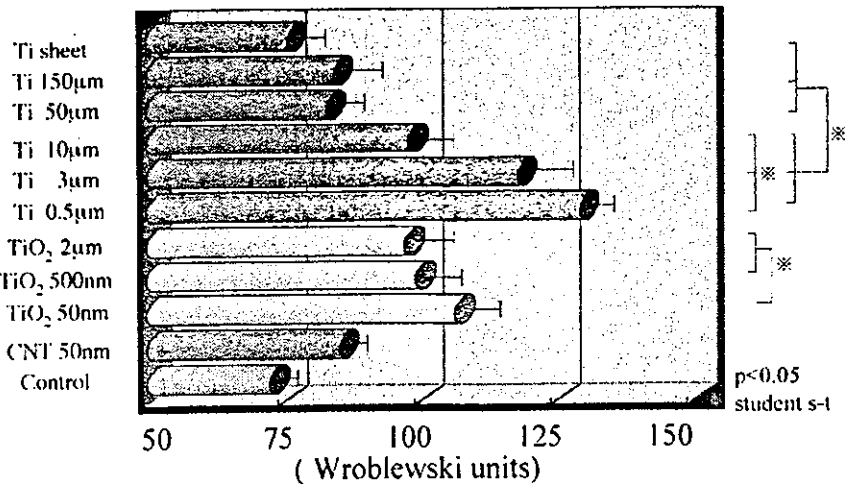

Fig.4 LDH activity

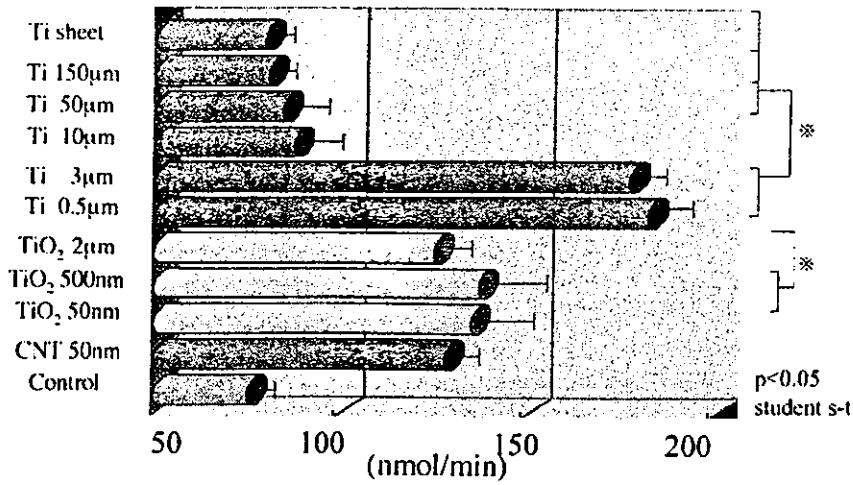

Fig.5 Superoxide anion

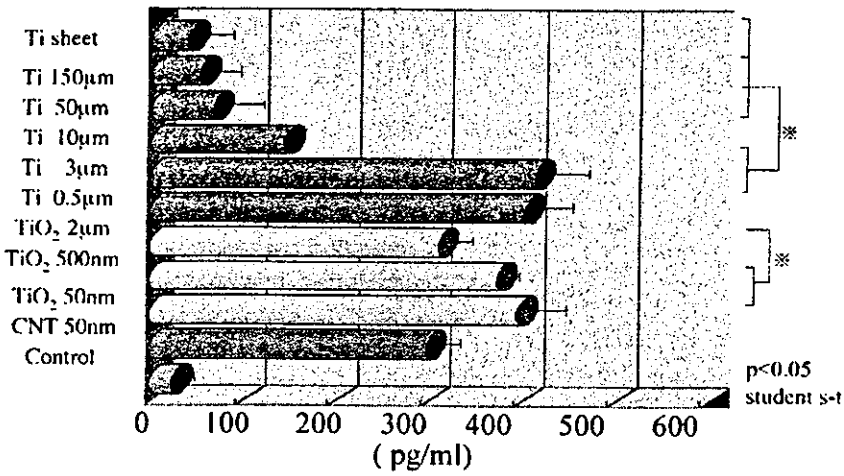

Fig.6 TNF-α

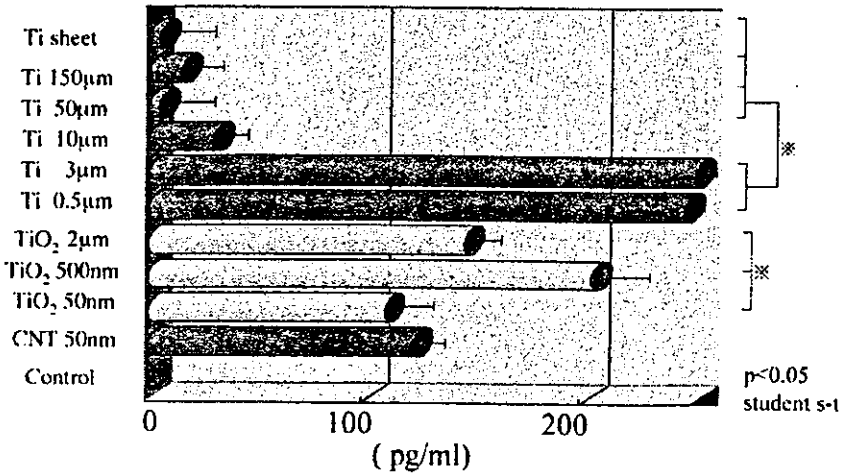

Fig.7 IL-1β

There is a clear difference in the emission of inflammatory cytokines for 3 μm and 10 μm (Fig.6). The distinct release of TNF- alpha was observed in 3 μm or less particles. There was no statistical difference of cytokines under 3 μm. The IL-1beta showed the similar (Fig.7).

SEM observation revealed the degenerative changes in the morphology of neutrophils (Fig.8). The activated neutrophils extended some pseudopods and phagocytized particles into the cytoplasm. 50nm TiO_2 particles and CNTs induced the morphological change of neutrophils. After 6 hours, the atrophied and destroyed neutrophils were observed.

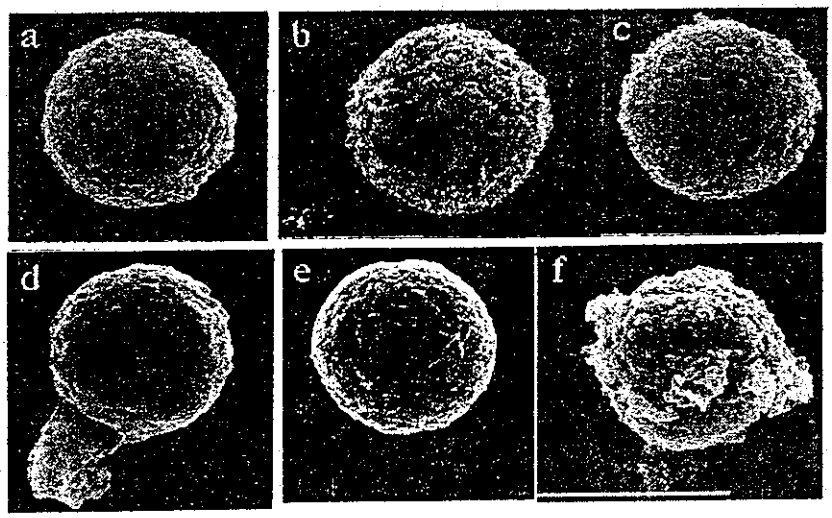

Fig.8
SEM images (Bar = 10 μm)
a: Neutrophil with HBSS
b: Activated by TiO_2 particles
c: Activated by CNTs
d: Extension of pseudopod and phagocytized particles
e: Atrophied neutrophil
f: Destroyed membrane

Discussions

The study clearly showed the cytotoxicity due to the particle size effect in Ti, TiO_2 and CNTs. Micro-nano particles may cause cytotoxicity, although the macroscopic size is quite biocompatible. The increased superoxide content *in vivo* may affect the cell circumference. The chemical mediators, TNF- alpha and IL-1beta, may induce the inflammatory cascade to affect tissue and organ. The effect is further pronounced by phagocytosis when particles are smaller than cells [7]. The clinical inflammatory reaction around the abrasion powders can be well understand by the results obtained in cell functional *in vitro* tests.

References

[1] K. Takamura, T. Yamada and Y. Sugioka, et al., J Biomed Mater Res: 28, p. 583-9.

[2] Young-kyun Yeo, Seoug-cheul Lim, et al., J Oral Maxillofac. Surg: 55, p. 322-326.

[3] A. Rosenberg, K.W. Grätz and H.F., Sailer J Oral Maxillofac. Surg: 22 , p. 185-188.

[4] Y. Tanimura, F. Watari, et al., J Oral and Maxillofacial Surgery: 46(11), p. 750.

[5] M. Uo, F. Watari, A. Yokoyama, T. Kawasaki, et al., Biomaterials: 20, p. 47-55

[6] F. Takesita, H. Tkata, Y. Ayukawa and T. Suetsugu, Biomaterials: 18 , p. 21-5

[7] Kazuchika Tamura, Fumio Watari, et al., Materials Transactions: 43(12), p.3052